

Advances in single-beacon one-way-travel-time acoustic navigation for underwater vehicles

Sarah E Webster^{1,2}, Ryan M Eustice³, Hanumant Singh⁴ and Louis L Whitcomb^{1,4}

Abstract

This paper reports the formulation and evaluation of a centralized extended Kalman filter designed for a novel navigation system for underwater vehicles. The navigation system employs Doppler sonar, depth sensors, synchronous clocks, and acoustic modems to achieve simultaneous acoustic communication and navigation. The use of a single moving reference beacon eliminates the requirement for the underwater vehicle to remain in a bounded navigable area; the use of underwater modems and synchronous clocks enables range measurements based on one-way time-of-flight information from acoustic data-packet broadcasts. The acoustic data packets are broadcast from a single, moving reference beacon and can be received simultaneously by multiple vehicles within acoustic range. We report results from a simulated deep-water survey and real field data collected from an autonomous underwater vehicle survey in 4000 m of water on the southern Mid-Atlantic Ridge with an independent long-baseline navigation system for ground truth.

Keywords

Marine robotics, localization, range sensing, sensor fusion

1. Introduction

This paper reports the formulation and experimental evaluation of a centralized extended Kalman filter (CEKF), which has access to both ship and vehicle sensor data, and is designed to implement single-beacon one-way-travel-time (OWTT) navigation for underwater vehicles. Single-beacon OWTT navigation employs Doppler sonar, pressure depth sensors, a gyrocompass, synchronous clocks, and acoustic modems to calculate range measurements based on the one-way travel-times of acoustic data packets, thereby enabling simultaneous acoustic communication and navigation. Our goal is to enable high-precision absolute navigation of underwater vehicles for missions with length scales on the order of 1–100 km without requiring fixed navigation reference beacons. Available strap-down sensors such as Doppler velocity logs (DVLs) and inertial measurement units (IMUs) measure vehicle velocities and accelerations, which can be integrated to estimate relative change in vehicle position. Unaided IMU and DVL navigation methods estimate local displacement with errors that are unbounded over time; thus they require auxiliary navigation methods to provide error correction and absolute georeferencing.

Traditional methods for achieving bounded-error navigation such as ultra-short baseline navigation (USBL) and tone-burst implementations of long baseline navigation (LBL) suffer from a lack of scalability because the rate at which multiple vehicles can receive navigation updates

decreases linearly as the number of navigated vehicles in the water increases (Hunt et al. 1974). In addition, conventional LBL navigation requires external, fixed reference beacons that limit the vehicle's navigable range to 5–10 km from the beacon network.

In contrast, OWTT navigation relies on ranges estimated from time-of-flight information of acoustic data packets between the vehicle and a reference beacon of known, though not necessarily stationary, location (Eustice et al. 2006, 2007; Webster et al. 2009b). This method provides both bounded-error position estimates and, with a moving reference beacon, long-range capabilities (e.g. on the order of 100 km) without the need for multiple, costly, fixed beacons. OWTT navigation provides scalability as well, allowing all vehicles within acoustic range to simultaneously use the same acoustic data packet broadcast, independent of the number of vehicles. Figure 1 depicts

¹Department of Mechanical Engineering, Johns Hopkins University

²Consortium for Ocean Leadership, Washington D.C.

³Department of Naval Architecture & Marine Engineering, University of Michigan

⁴Department of Applied Ocean Physics & Engineering, Woods Hole Oceanographic Institution

Corresponding author:

Sarah Webster, 3400 North Charles Street, 223 Latrobe Hall, Baltimore, 21218, USA.

Email: swebster@jhu.edu



Fig. 1. Acoustic data-packets broadcast from the ship can be used for combined communication and navigation by multiple underwater vehicles. Image credit: Paul Oberlander, WHOI.

a ship-based acoustic modem broadcasting acoustic data packets to multiple underwater vehicles.

In the deep-water survey presented herein, the ship and vehicle communicated acoustically via Woods Hole Oceanographic Institution (WHOI) micro-modems using 32-byte binary acoustic data packets (Freitag et al. 2005). The micro-modems support a synchronous navigation mode in which the modem is configured to begin transmission of acoustic data packets at the top of the second. We encode the time of launch (TOL) along with information about the sender's geodetic location in the acoustic data packet. The time of arrival (TOA) of the acoustic data packet at the receiver, the decoded TOL and position information in the acoustic data packet, and the sound velocity profile of the local water column are used to estimate range. Between range measurements, vehicle position is estimated using depth, velocity, and attitude measurements.

Because the time-of-flight (TOF) measurement is based on the difference between the sender's time and the receiver's time, it is crucial that the clocks on the sender and the receiver are synchronized to within an acceptable tolerance throughout the dive. During the deep-water survey, the acoustic communications system, called Acomms, provided subsea precision timing support as well as controlling all acoustic communications. The Acomms system has underwater acoustic modems; precision, synchronized clocks on both the vehicle and the reference beacon (in our case the ship); and custom stand-alone software necessary to support both modem operations and the required precision timing functionality (Webster et al. 2009a).

The goal of this work is to report a principled, general approach to tracking correlation and time delays for

the purposes of OWTT navigation utilizing a centralized delayed-state extended Kalman filter (EKF), and to evaluate this method in the context of a two-node marine application with experimental deep-water survey data. This approach represents the uncertainty of the vehicle processes, the navigation sensor observations, the state of both the vehicle and the ship, as well as the correlation between vehicle and ship states. Including both ship and vehicle states in the state vector enables the algorithm to properly model range measurements between the current vehicle state and an historic ship state. This approach provides substantial benefits in implementations where there is non-negligible mutual correlation between the ship and the vehicle (Walls and Eustice 2011). This approach also provides a framework that can be extended to a fully decentralized, multi-vehicle navigation algorithm, in which range measurements between vehicles can be incorporated without causing overconfident position estimates (Webster et al. 2010).

In the centralized implementation reported herein, the algorithm requires concurrent access to both ship and vehicle sensor data, which limits the centralized algorithm to use in post-processing. Because the algorithm has access to all sensor data, it will provide the best possible estimate of vehicle position *within the Kalman-filter framework*, compared to decentralized algorithms that rely on delayed or incomplete sensor data to prevent overconfidence. Thus the centralized implementation provides a benchmark for future work on Kalman-filter-based decentralized single-beacon navigation algorithms.

The remainder of this paper is organized as follows: Section 2 describes previous work in the area of single-beacon navigation based on range measurements. Section 3 reports the mathematical framework for the CEKF for OWTT navigation. Section 4 describes and reports results from a simulated deep-water survey, while Section 5 describes and reports results from the actual deep-water field trials. Section 6 offers some concluding discussion.

2. Previous work

The majority of the prior literature in the area of single-beacon navigation reports the results of numerical simulations of the algorithms proposed therein. Only a few report experimental evaluations of the proposed algorithms, and even fewer employ independent navigation methods to evaluate quantitatively the accuracy of the proposed methods. Previous work in the area of single-beacon navigation is extensively reviewed in Webster (2010). This section reviews some of the references most relevant to this paper.

The earliest formulation of underwater vehicle navigation using ranges from a single beacon that is known to the authors is reported in Scherbatyuk (1995). This approach employs least-squares to solve for the vehicle's unknown initial position and a constant-velocity unknown current; additionally, a linear algebra-based observability analysis is reported. More recent least-squares solutions are reported in Hartsfield (2005) and LaPointe (2006), the former using

ad hoc iterative techniques to estimate course, the latter reporting a method for advancing multiple single-beacon fixes along the vehicle's estimated trackline to simulate a multi-beacon fix.

Range-only localization methods used for estimating the position of a target are addressed by Ristic et al. (2002) and Song (1999). In Ristic et al. (2002) the authors compute the theoretical Cramér–Rao lower bound and compare it to the performance of a maximum-likelihood estimator (MLE), an EKF, and a regularized particle filter during field tests. In Song (1999) the author addresses the observability of the target-tracker problem using the Fisher information matrix and reports simulation results using an EKF. In related work Alleyne (2000) implements the EKF from Song (1999) and reports simulation results. The use of EKFs for homing and single-beacon navigation, initialized by least-squares, is reported in Baccou and Jouvencel (2002, 2003) and Vaganay et al. (2000) for both simulation and field trials. In Baccou and Jouvencel (2003) the authors also report a simulated two-vehicle system using a cascaded approach in which the second vehicle navigates relative to the first vehicle using inter-vehicle range measurements. Larsen (2000, 2001, 2002) report an error state EKF for single-beacon navigation based on error models of the vehicle's inertial navigation system. The authors report results using a combination of field and simulation data. A method of navigation using synchronous acoustic beacons and one-way travel times to calculate range-rate is discussed in Singh et al. (2001).

The recently published work, Morice and Veres (2011), report geometric bounding techniques and simulation results for range-based underwater navigation. The work reported in McPhail and Pebody (2009) is one of the few to address range-based positioning in deep water and reports both simulation and experimental results. This work uses a ship-based ranging system to obtain an accurate initial position for the vehicle. Once computed, the position fix is acoustically broadcast to the vehicle before the vehicle carries out its intended mission using dead-reckoning.

Several different methods for addressing the observability of single-beacon range-only navigation are reported in the literature. Gadre (2007) and Gadre and Stilwell (2004, 2005a,b) report an observability analysis employing limiting systems to assess uniform observability, and derive sufficient conditions for the existence of an observer with exponentially decaying estimation error for the cases of both known and unknown ambient currents. The authors report field results from their implementation of an EKF. In related work, Lee et al. (2008) extend the EKF reported in Gadre (2007) and Gadre and Stilwell (2004, 2005a,b) to three-dimensional coordinates with simulation results. A concise observability analysis in continuous time using Lie derivatives to compute conditions for which the system has local weak observability is reported in Ross and Jouffroy (2005). In Jouffroy and Reger (2006) the

authors report an algebraic analysis showing local uniform observability based on signal estimation techniques, though the lack of an estimation model disallows the computation of an updated position in the absence of a new measurement.

Bahr and Leonard (2006) and Bahr (2009) address cooperative localization of multiple underwater and surface vehicles using vehicle-based EKFs. One-way travel times are garnered from acoustically broadcast mean and covariance estimates to perform range measurements from multiple references. Fallon et al. (2010) extend this work to consider navigation in the context of a single reference beacon and compare the performance of a particle filter, a non-linear least-squares estimator, and an EKF with experimental data. Similar to our work, the authors of Fallon et al. (2010) rely on a single moving georeferenced beacon to support the localization of multiple vehicles through asynchronous acoustic broadcasts. The main difference between the algorithm used in Fallon et al. (2010) and the algorithm presented herein, is that Fallon et al. (2010) employ a vehicle-based EKF and perform range measurement updates using the absolute position and covariance broadcast from the reference beacon. One of the benefits of this formulation is that the algorithm is applicable in real time. However, excluding the reference beacon position from the state vector ignores the potential mutual correlation between the reference beacon and the vehicle, making the algorithm unsuitable for applications in which substantial correlation is expected. Correlation is not a significant source of error for deployments for which the algorithm presented in Fallon et al. (2010) is intended, where the reference beacon has precise knowledge of its position through access to GPS and there are no inter-vehicle ranges. Interesting and useful scenarios do exist, though, that would incur significant mutual correlation. Walls and Eustice (2011) report a comparative experimental evaluation of three different approaches to distributed state estimation for synchronous-clock one-way travel-time navigation. The experimental evaluations reported in Walls and Eustice (2011) show that, under some communication topologies, distributed implementations of the Kalman filter that do not account for measurement correlation can result in state estimates that differ significantly from approaches in which measurement correlation is explicitly accounted for. In Bahr (2009), the work upon which Fallon et al. (2010) is based, a multi-hypothesis strategy is employed to avoid overconfidence by preventing measurement data from being incorporated multiple times, but this approach is cumbersome due to tracking the multiple hypotheses.

The work reported in this paper extends the work reported in Eustice et al. (2006) and Eustice et al. (2007), which employ a maximum-likelihood estimator and report the theory and shallow-water experimental results for OWTT navigation.

3. Centralized extended Kalman filter

An EKF is employed to fuse depth, gyrocompass, and Doppler velocity measurements from the vehicle; position and attitude measurements from the ship; and range measurements between the vehicle and the ship. The CEKF employed herein for single-beacon navigation estimates the current and previous states of both the ship and the vehicle and is applicable in post-processing of previously acquired dive data. This section contains the details of our centralized implementation for OWT navigation, summarized in Algorithm 1. A description of the state vector is presented in Section 3.1, details of the vehicle process model in Section 3.2, the ship process model in Section 3.3, process prediction and augmentation in Section 3.4, and the measurement models in Section 3.5. Appendix A contains a brief review of the EKF.

Algorithm 1 CEKF with state augmentation

```

1: loop {perform prediction and measurement update}
2:   calculate time step for prediction:
      $\Delta t = \min[\text{time until top of the second; time until}$ 
      $\text{next measurement; } 0.1\text{s (10 Hz pred.)}]$ 
3:   if current time == top-of-second then
4:     augment state vector with current state while per-
     forming process prediction  $\Delta t$ , equations (29),
     (30)
5:   else
6:     perform process prediction  $\Delta t$  without augment-
     ing state vector, equations (26), (27)
7:   end if
8:   if  $\exists$  measurements at new time step then
9:     perform measurement update, equations (42), (43)
10:  end if
11: end loop
  
```

3.1. State description

The complete state vector for this implementation of the CEKF, denoted herein by the bold font \mathbf{x} , consists of the current vehicle estimate, \mathbf{x}_v , the current ship estimate, \mathbf{x}_s , and a fixed-length queue of historic states representing the ship and vehicle positions at the beginning of each second (referred to as the top of the second) for the most recent n seconds, denoted \mathbf{x}_{v-i} and \mathbf{x}_{s-i} for $i \in [1, \dots, n]$

$$\mathbf{x} = [\mathbf{x}_v^\top, \mathbf{x}_s^\top, \mathbf{x}_{v-1}^\top, \mathbf{x}_{s-1}^\top, \dots, \mathbf{x}_{v-n}^\top, \mathbf{x}_{s-n}^\top]^\top. \quad (1)$$

The current ship state contains the ship's xy position, heading, and the respective velocities

$$\mathbf{x}_s = [x_s, y_s, \theta_s, \dot{x}_s, \dot{y}_s, \dot{\theta}_s]^\top. \quad (2)$$

The current vehicle state contains pose and attitude, as well as body-frame linear and angular velocities

$$\mathbf{x}_v = [\mathbf{s}^\top, \boldsymbol{\varphi}^\top, \mathbf{v}^\top, \boldsymbol{\omega}^\top]^\top \quad (3)$$

$$\mathbf{s} = \begin{bmatrix} x \\ y \\ z \end{bmatrix}, \boldsymbol{\varphi} = \begin{bmatrix} \phi \\ \theta \\ \psi \end{bmatrix}, \mathbf{v} = \begin{bmatrix} u \\ v \\ w \end{bmatrix}, \boldsymbol{\omega} = \begin{bmatrix} p \\ q \\ r \end{bmatrix} \quad (4)$$

where \mathbf{s} is the vehicle pose in the local frame, $\boldsymbol{\varphi}$ is the vehicle attitude (Euler roll, pitch, and heading), \mathbf{v} is the body-frame linear velocity, and $\boldsymbol{\omega}$ is the body-frame angular velocity.

The historic states contain full estimates of the vehicle's state and the ship's state from previous time steps. Historic states are necessary for causal processing of range measurements because of the time required for an acoustic data packet to propagate from the sender to the receiver. When the acoustic modems are in synchronous navigation mode all acoustic transmissions are initiated at the top of the second. Thus, in order to ensure that the state vector contains the appropriate historic states needed to model range measurement updates, the CEKF maintains an estimate of the state of the system at the top of the second for the previous n seconds. In practice $n = 6$ for this implementation, which enables the algorithm to accommodate range measurements with travel times of up to six seconds, which is equivalent to approximately a 9-km-range measurement. Note that while this framework allows range measurements to be made every second, in practice, due to the limitation of the acoustic channel (and hardware limitations on the amount of time required to transmit the acoustic data packets), range measurements are not typically made every second.

3.2. Vehicle process model

The reported CEKF uses a constant-velocity process model for the vehicle, which is defined as

$$\dot{\mathbf{x}}_v = \underbrace{\begin{bmatrix} \mathbf{0} & \mathbf{0} & \mathbf{R}(\boldsymbol{\varphi}) & \mathbf{0} \\ \mathbf{0} & \mathbf{0} & \mathbf{0} & \mathcal{J}(\boldsymbol{\varphi}) \\ \mathbf{0} & \mathbf{0} & \mathbf{0} & \mathbf{0} \\ \mathbf{0} & \mathbf{0} & \mathbf{0} & \mathbf{0} \end{bmatrix}}_{\mathbf{f}(\mathbf{x}_v(t))} \mathbf{x}_v + \underbrace{\begin{bmatrix} \mathbf{0} & \mathbf{0} \\ \mathbf{0} & \mathbf{0} \\ \mathbf{I} & \mathbf{0} \\ \mathbf{0} & \mathbf{I} \end{bmatrix}}_{\mathbf{G}_v} \mathbf{w}_v \quad (5)$$

where $\mathbf{R}(\boldsymbol{\varphi})$ is the transformation from body-frame to local-level linear velocities, $\mathcal{J}(\boldsymbol{\varphi})$ is the transformation from body-frame angular velocities to Euler rates, and $\mathbf{w}_v \sim \mathcal{N}(\mathbf{0}, \mathbf{Q}_v)$ is zero-mean Gaussian process noise in the acceleration term. $\mathbf{R}(\boldsymbol{\varphi})$ and $\mathcal{J}(\boldsymbol{\varphi})$ are found by solving

$$\mathbf{R}(\boldsymbol{\varphi}) = \mathbf{R}_\psi^\top \mathbf{R}_\theta^\top \mathbf{R}_\phi^\top \quad (6)$$

where

$$\mathbf{R}_\psi = \begin{bmatrix} \cos \psi & \sin \psi & 0 \\ -\sin \psi & \cos \psi & 0 \\ 0 & 0 & 1 \end{bmatrix}, \mathbf{R}_\theta = \begin{bmatrix} \cos \theta & 0 & -\sin \theta \\ 0 & 1 & 0 \\ \sin \theta & 0 & \cos \theta \end{bmatrix}, \quad (7)$$

$$\mathbf{R}_\phi = \begin{bmatrix} 1 & 0 & 0 \\ 0 & \cos \phi & \sin \phi \\ 0 & -\sin \phi & \cos \phi \end{bmatrix}$$

and

$$\begin{aligned}\boldsymbol{\omega} &= \begin{bmatrix} \dot{\phi} \\ 0 \\ 0 \end{bmatrix} + R_\phi \begin{bmatrix} 0 \\ \dot{\theta} \\ 0 \end{bmatrix} + R_\phi R_\theta \begin{bmatrix} 0 \\ 0 \\ \dot{\psi} \end{bmatrix} \\ &= \underbrace{\begin{bmatrix} 1 & 0 & -\sin \theta \\ 0 & \cos \phi & \sin \phi \cos \theta \\ 0 & -\sin \phi & \cos \phi \cos \theta \end{bmatrix}}_{\mathcal{J}^{-1}} \dot{\boldsymbol{\phi}}\end{aligned}\quad (8)$$

$$\mathcal{J} = \begin{bmatrix} 1 & \sin \phi \tan \theta & \cos \phi \tan \theta \\ 0 & \cos \phi & -\sin \phi \\ 0 & \sin \phi \sec \theta & \cos \phi \sec \theta \end{bmatrix}. \quad (9)$$

Note that the vehicle process model does not include a control input term $\mathbf{u}(t)$ because we do not assume a dynamic model for the vehicle. The use of a simple kinematic model makes the algorithm trivially applicable to any vehicle.

We linearize the vehicle process model, equation (5), about $\boldsymbol{\mu}_v$, our estimate of the vehicle state at time t , using the Taylor series expansion

$$\begin{aligned}\dot{\mathbf{x}}_v(t) &= \mathbf{f}(\boldsymbol{\mu}_v) + \mathbf{F}_v(\mathbf{x}_v(t) - \boldsymbol{\mu}_v) \\ &\quad + HOT + \mathbf{G}_v \mathbf{w}_v(t)\end{aligned}\quad (10)$$

where

$$\mathbf{F}_v = \left. \frac{\partial \mathbf{f}(\mathbf{x}_v)}{\partial \mathbf{x}_v} \right|_{\mathbf{x}_v(t)=\boldsymbol{\mu}_v} \quad (11)$$

and *HOT* denotes higher-order terms. Dropping the *HOT* and rearranging we get

$$\dot{\mathbf{x}}_v(t) \approx \mathbf{F}_v \mathbf{x}_v(t) + \underbrace{\mathbf{f}(\boldsymbol{\mu}_v) - \mathbf{F}_v \boldsymbol{\mu}_v}_{\mathbf{u}_v(t)} + \mathbf{G}_v \mathbf{w}_v(t) \quad (12)$$

$$= \mathbf{F}_v \mathbf{x}_v(t) + \mathbf{u}_v(t) + \mathbf{G}_v \mathbf{w}_v(t) \quad (13)$$

where $\mathbf{f}(\boldsymbol{\mu}_v) - \mathbf{F}_v \boldsymbol{\mu}_v$ is treated as a constant pseudo-input term $\mathbf{u}_v(t)$.

In order to discretize the linearized vehicle process model we rewrite equation (13) as

$$\dot{\mathbf{x}}_v(t) = \mathbf{F}_v \mathbf{x}_v(t) + \mathbf{B}_v \mathbf{u}_v(t) + \mathbf{G}_v \mathbf{w}_v(t) \quad (14)$$

where $\mathbf{B}_v = \mathbf{I}$. Assuming zero-order hold and using the standard method (Bar-Shalom et al. 2001) to discretize over a time step T we solve for \mathbf{F}_{v_k} and \mathbf{B}_{v_k} in the discrete form of the process model

$$\mathbf{x}_{v_{k+1}} = \mathbf{F}_{v_k} \mathbf{x}_{v_k} + \mathbf{B}_{v_k} \mathbf{u}_k + \mathbf{w}_{v_k} \quad (15)$$

$$\mathbf{F}_{v_k} = e^{\mathbf{F}_v T} \quad (16)$$

$$\begin{aligned}\mathbf{B}_{v_k} &= \int_0^T e^{\mathbf{F}_v(T-\tau)} \mathbf{B}_v d\tau \\ &= e^{\mathbf{F}_v T} \int_0^T e^{-\mathbf{F}_v \tau} d\tau.\end{aligned}\quad (17)$$

The discretized process noise \mathbf{w}_{v_k} has the form

$$\mathbf{w}_{v_k} = \int_0^T e^{\mathbf{F}_v(T-\tau)} \mathbf{G}_v \mathbf{w}_v(\tau) d\tau \quad (18)$$

for which we can calculate the mean and variance

$$\begin{aligned}E[\mathbf{w}_{v_k}] &= E\left[\int_0^T e^{\mathbf{F}_v(T-\tau)} \mathbf{G}_v \mathbf{w}_v(\tau) d\tau\right] \\ &= \int_0^T e^{\mathbf{F}_v(T-\tau)} \mathbf{G}_v E[\mathbf{w}_v(\tau)] d\tau \\ &= 0\end{aligned}\quad (19)$$

$$\begin{aligned}\mathbf{Q}_{v_k} &= E[\mathbf{w}_{v_k} \mathbf{w}_{v_k}^\top] \\ &= \int_0^T e^{\mathbf{F}_v(T-\tau)} \mathbf{G}_v \mathbf{Q}_v \mathbf{G}_v^\top e^{\mathbf{F}_v^\top(T-\tau)} d\tau.\end{aligned}\quad (20)$$

The details of the derivation of \mathbf{Q}_{v_k} are in Appendix B.

3.3. Ship process model

The reported CEKF uses a linear constant-velocity process model for the ship, which is defined as

$$\dot{\mathbf{x}}_s = \underbrace{\begin{bmatrix} \mathbf{0} & \mathbf{I} \\ \mathbf{0} & \mathbf{0} \end{bmatrix}}_{\mathbf{F}_s} \mathbf{x}_s + \underbrace{\begin{bmatrix} \mathbf{0} \\ \mathbf{I} \end{bmatrix}}_{\mathbf{G}_s} \mathbf{w}_s \quad (21)$$

where $\mathbf{w}_s \sim \mathcal{N}(0, \mathbf{Q}_s)$ is zero-mean Gaussian process noise in the acceleration term, which is independent of the vehicle process noise \mathbf{w}_v defined in equation (5). Because the ship process model is already linear it does not require linearization.

The ship process model, is discretized in the same fashion as the vehicle process model

$$\mathbf{x}_{s_{k+1}} = \mathbf{F}_{s_k} \mathbf{x}_{s_k} + \mathbf{w}_{s_k} \quad (22)$$

$$\mathbf{F}_{s_k} = e^{\mathbf{F}_s T} \quad (23)$$

$$\begin{aligned}&= \mathbf{I} + \mathbf{F}_s T + \frac{1}{2} \mathbf{F}_s^2 T^2 + \frac{1}{3} \mathbf{F}_s^3 T^3 + \dots \\ &= \begin{bmatrix} \mathbf{I} & \mathbf{I}T \\ \mathbf{0} & \mathbf{I} \end{bmatrix}\end{aligned}$$

where the higher-order terms are *identically zero* because of the structure of \mathbf{F}_s , resulting in a simple closed-form solution for \mathbf{F}_{s_k} . Note that $\mathbf{B}_{s_k} = \mathbf{0}$ because $\mathbf{B}_s = \mathbf{0}$. The ship's discretized process noise

$$\mathbf{w}_{s_k} = \int_0^T e^{\mathbf{F}_s(T-\tau)} \mathbf{G}_s \mathbf{w}_s(\tau) d\tau \quad (24)$$

can also be shown to be zero-mean Gaussian using formulas (19) and (20), such that $\mathbf{w}_{s_k} \sim \mathcal{N}(0, \mathbf{Q}_{s_k})$. Due to the structure of \mathbf{F}_{s_k} , the covariance matrix simplifies to

$$\mathbf{Q}_{s_k} = \begin{bmatrix} \frac{1}{2} T^3 & \frac{1}{2} T^2 \\ \frac{1}{2} T^2 & T \end{bmatrix} \mathbf{Q}_s. \quad (25)$$

3.4. Process prediction and augmentation

The complete state process prediction is written in terms of the full state vector of the system defined in equation (1). Combining the discrete-time linearized vehicle and ship process models, equations (15) and (22), and substituting them into the discrete-time linearized Kalman process prediction equation (40), the complete state process prediction becomes

$$\boldsymbol{\mu}_{k+1|k} = \underbrace{\begin{bmatrix} \mathbf{F}_{v_k} & 0 & 0 & \cdots & 0 \\ 0 & \mathbf{F}_{s_k} & 0 & \cdots & 0 \\ 0 & 0 & \mathbf{I} & \cdots & 0 \\ \vdots & \vdots & \vdots & \ddots & \vdots \\ 0 & 0 & 0 & \cdots & \mathbf{I} \end{bmatrix}}_{\mathbf{F}_k} \boldsymbol{\mu}_{k|k} + \begin{bmatrix} \mathbf{B}_{v_k} \mathbf{u}_k \\ 0 \\ 0 \\ \vdots \\ 0 \end{bmatrix} \quad (26)$$

$$\boldsymbol{\Sigma}_{k+1|k} = \mathbf{F}_k \boldsymbol{\Sigma}_{k|k} \mathbf{F}_k^\top + \mathbf{Q}_k \quad (27)$$

where $\boldsymbol{\mu}$ and $\boldsymbol{\Sigma}$ are the mean and covariance, respectively, of the estimate of the state \mathbf{x} and

$$\mathbf{Q}_k = \begin{bmatrix} \mathbf{Q}_{v_k} & 0 & 0 & \cdots & 0 \\ 0 & \mathbf{Q}_{s_k} & 0 & \cdots & 0 \\ 0 & 0 & 0 & \cdots & 0 \\ \vdots & \vdots & \vdots & \ddots & \vdots \\ 0 & 0 & 0 & \cdots & 0 \end{bmatrix}. \quad (28)$$

Note that the historic states do not change during this process update.

A modified process prediction is necessary at the top of the second when state augmentation is done in concert with process prediction. During this modified prediction step, in addition to predicting forward the current vehicle state, the estimate of the current state (before the prediction) is augmented to the state vector while simultaneously marginalizing out the oldest historic state (\mathbf{x}_{v-n} and \mathbf{x}_{s-n}) and \mathbf{Q}_k is defined as before,

$$\boldsymbol{\mu}_{k+1|k} = \underbrace{\begin{bmatrix} \mathbf{F}_{v_k} & 0 & 0 & \cdots & 0 & 0 & 0 \\ 0 & \mathbf{F}_{s_k} & 0 & \cdots & 0 & 0 & 0 \\ \mathbf{I} & 0 & 0 & \cdots & 0 & 0 & 0 \\ 0 & \mathbf{I} & 0 & \cdots & 0 & 0 & 0 \\ 0 & 0 & \mathbf{I} & \cdots & 0 & 0 & 0 \\ \vdots & \vdots & \vdots & \ddots & \vdots & \vdots & \vdots \\ 0 & 0 & 0 & \cdots & \mathbf{I} & 0 & 0 \end{bmatrix}}_{\tilde{\mathbf{F}}_k} \boldsymbol{\mu}_{k|k} + \begin{bmatrix} \mathbf{B}_{v_k} \mathbf{u}_k \\ 0 \\ 0 \\ 0 \\ 0 \\ \vdots \\ 0 \end{bmatrix} \quad (29)$$

$$\boldsymbol{\Sigma}_{k+1|k} = \tilde{\mathbf{F}}_k \boldsymbol{\Sigma}_{k|k} \tilde{\mathbf{F}}_k^\top + \mathbf{Q}_k. \quad (30)$$

3.5. Measurement models

The range measurement from the ship's modem transducer to the vehicle's modem transducer is a non-linear function of the current vehicle state and an historic ship state. For simplicity of notation, we assume here, without loss

of generality, that the transducers are located at the origin of their respective local frames. In the actual implementation the offsets of the transducers from their respective origins are taken into account, including the effect of the ship's pitch and roll on transducer position. Because ship pitch and roll are not included in the state vector, we interpolate the ship's pitch and roll at the time of launch of the acoustic data packet using pitch and roll data from the ship's gyrocompass, and use that along with the transducer offset to calculate the relative position of the ship's transducer. The measurement equation for a range measurement made from an acoustic data packet sent from the ship to the vehicle is

$$z_{\text{rng}} = \sqrt{(\mathbf{x}_{v_{xyz}} - \mathbf{x}_{s_{xyz}})^\top (\mathbf{x}_{v_{xyz}} - \mathbf{x}_{s_{xyz}})} + v_{\text{rng}} \quad (31)$$

where $\mathbf{x}_{s_{xyz}}$ is the ship pose at the time of launch, t_{TOL} , of the acoustic data packet and $\mathbf{x}_{v_{xyz}}$ is the vehicle pose at the time of arrival, t_{TOA} , of the acoustic data packet. We assume zero-mean Gaussian measurement noise, $v_{\text{rng}} \sim \mathcal{N}(0, R_{\text{rng}})$, which is in units of distance and represents the imprecision in timing multiplied by the depth-averaged sound velocity between the two transducers. The covariance R_{rng} is assumed to be identical for all range measurements and therefore does not have the time-dependent subscript k . The validity of these assumptions for the the range measurement error are addressed in more detail in Section 5.7. We can rewrite equation (31) in terms of the state vector as

$$z_{\text{rng}} = (\mathbf{x}^\top \mathbf{M}^\top \mathbf{M} \mathbf{x})^{\frac{1}{2}} + v_{\text{rng}} \quad (32)$$

where

$$\mathbf{M} = \begin{bmatrix} \mathbf{J}_v & 0 & \cdots & 0 & \mathbf{J}_s & 0 & \cdots & 0 \end{bmatrix}. \quad (33)$$

In \mathbf{M} , \mathbf{J}_v is defined to capture the pose information of the vehicle, $\mathbf{x}_v(t_{\text{TOA}})$, at the time of arrival of the acoustic broadcast and \mathbf{J}_s is defined to capture the pose information of the ship, $\mathbf{x}_s(t_{\text{TOL}})$, at the time of launch of the acoustic broadcast. The Jacobian of the range measurement, equation (32), at t_k with respect to \mathbf{x} is

$$\begin{aligned} \mathbf{H}_{\text{rng}_k} &= \left. \frac{\partial z_{\text{rng}}(\mathbf{x})}{\partial \mathbf{x}} \right|_{\mathbf{x}=\boldsymbol{\mu}_{k|k-1}} \\ &= (\boldsymbol{\mu}_{k|k-1}^\top \mathbf{M}^\top \mathbf{M} \boldsymbol{\mu}_{k|k-1})^{-\frac{1}{2}} \boldsymbol{\mu}_{k|k-1}^\top \mathbf{M}^\top \mathbf{M}. \end{aligned} \quad (34)$$

This observation model also applies to range measurements made from the vehicle to the ship by substituting the vehicle pose at the time of launch and the ship pose at the time of arrival.

Measurements from additional navigation sensors are processed asynchronously using standard observation models (Eustice 2005). On the vehicle, the depth sensor provides observations of the vehicle's depth in the local-level coordinate frame. The velocity sensor, a Doppler velocity log, provides observations of the seafloor-relative velocity of the vehicle in the sensor coordinate frame. The OCTANS

gyrocompass provides observations of the vehicle's local-level attitude and body-frame angular rates. We assume zero-mean, Gaussian noise for all of these sensor measurements with standard deviations commensurate with the specifications of the instrument manufacturers.

Onboard the ship, a GPS provides observations of the position of the ship in the local-level coordinate frame. The ship's gyro provides observations of the ship's attitude in the local-level coordinate frame. We assume zero-mean, Gaussian noise for these sensor measurements as well. GPS measurements may be subject to correlation and drift as a result of variations in the satellite constellation over the course of the dive. The possible effects of this are addressed in Section 5.7.

4. Simulation

For comparison purposes, this simulation is designed to mimic the experimental setup of the deep-water survey presented in Section 5. In the simulated mission presented here, the vehicle drives ten 700-m tracklines spaced 80 m apart at a velocity of 0.35 m/s. The vehicle's depth is constant at 3800 m. The vehicle takes approximately 6 hours to complete the survey, during which time the ship drives around the vehicle's survey area in a diamond pattern at 0.5 m/s, broadcasting acoustic data packets every 2.5 minutes.

4.1. Simulated sensors

We assume that the ship data comprises simulated sensor data comparable to a differential global positioning system (DGPS) receiver and a gyrocompass to measure heading. The vehicle data comprises simulated sensor data comparable to an OCTANS fiber-optic gyrocompass to measure attitude and attitude rates; a Paroscientific pressure sensor to measure depth; and an RDI Doppler velocity log (DVL) to measure bottom-referenced velocities. Simulated range measurements comparable to those from acoustic modems are used to measure the range between the ship and the vehicle. The simulated vehicle and ship navigation sensors, their sampling frequencies, and the noise statistics for each sensor are summarized in Table 1.

4.2. Simulation results

To investigate the effect of range measurements on the CEKF's estimate of the vehicle trajectory, the simulation was run both with and without range measurements. In both cases the vehicle position was initialized with the same variance in x and y as the experimental data. Figure 2 shows the range-aided estimated vehicle trajectory (with $3\text{-}\sigma$ covariance ellipses) compared to the true vehicle trajectory over the course of the simulated dive. The simulated GPS-reported trajectory of the ship as it moves above the vehicle survey area is also shown. The distribution of the difference between the range-aided estimate of vehicle

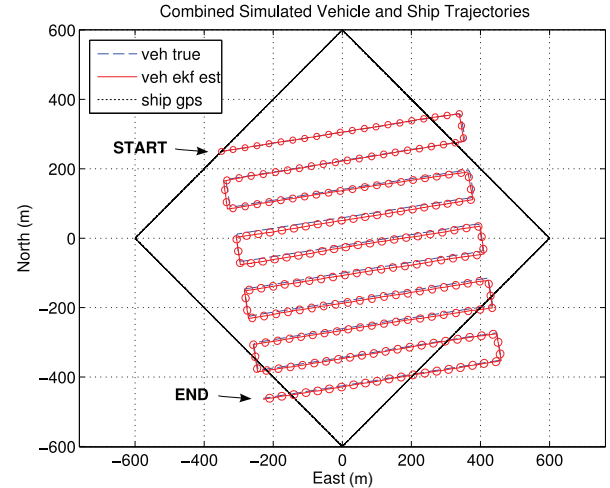


Fig. 2. In a simulated 6-hour, deep-water dive, the vehicle follows a typical survey trajectory while the ship moves counter-clockwise around a diamond-shaped trajectory, starting at the eastern-most apex.

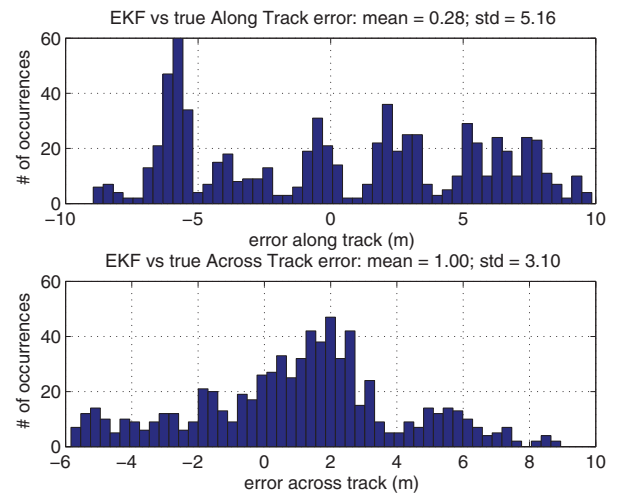


Fig. 3. The distribution of the along-track and across-track components of the estimated vehicle position error over the course of the range-aided simulated dive.

position and the true vehicle position over the course of the simulated dive can be seen in Figure 3.

The difference between the dead-reckoned vehicle trajectory versus the range-aided vehicle trajectory is not easily discernible on the scale of the x - y plot in Figure 2. Instead, Figure 4 shows the error in both the dead-reckoned and the range-aided vehicle trajectories compared to the true vehicle trajectory, plotted against their respective $3\text{-}\sigma$ bounds. The error between the trajectories and the true state stay within their $3\text{-}\sigma$ bounds for all but a few points and the range-aided trajectory clearly has smaller variance than the dead-reckoned trajectory. We can also represent spatial uncertainty in the filter by taking the determinant of the x - y portion of the covariance matrix to find the equivalent of

Table 1. Simulated navigation sensor sampling frequency and noise.

| Sensor | Frequency | Noise |
|---------------------|---------------|---------------------------------------------------------------------------------------------------|
| OCTANS ^a | 3.0 Hz | ψ, ϕ, θ : 0.5° r : $0.6^\circ/\text{s}$ p, q : $0.4^\circ/\text{s}$ |
| Depth sensor | 0.9 Hz | 6 cm |
| DVL | 3.0 Hz | 1 cm/s |
| GPS | 1.0 Hz | 0.5 m |
| Gyrocompass | 2.0 Hz | 0.05° |
| Modem | every 2.5 min | 3.3 m |

^a ψ , θ , and ϕ are local-level heading, pitch, and roll, respectively; r , q , and p are body-frame angular velocities for heading, pitch, and roll.

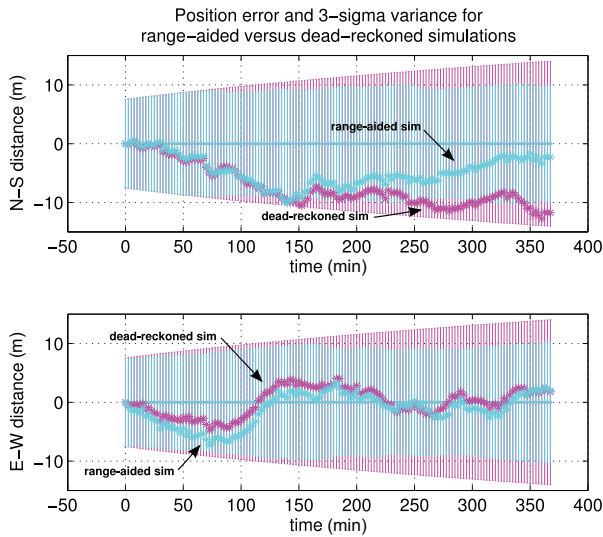


Fig. 4. The error between the range-aided simulation and the dead-reckoned simulation are shown compared to their associated $3\text{-}\sigma$ bounds. The state estimates of both remain inside their respective $3\text{-}\sigma$ error bounds except for a few points and the range-aided sigma bounds clearly shrink with time compared to the dead-reckoned $3\text{-}\sigma$ bounds (as expected).

a volume of uncertainty with units m^4 . Plotting the fourth root of this determinant gives us a representation of the spatial uncertainty in meters. Figure 5 shows this spatial uncertainty for both trajectories. As expected, the spatial uncertainty in the dead-reckoned track increases monotonically over time, while the range-aided trajectory has bounded uncertainty as a result of the range measurements.

To investigate the consistency of the filter we looked at the innovations of the sensor measurements. Figure 6 shows histograms of the innovations of the simulated velocity measurements from the DVL. The innovations of the DVL measurements are zero-mean and Gaussian indicating a consistent filter. Figure 7 shows the innovations of the range measurements over time. All innovations are well within the $3\text{-}\sigma$ innovation covariance bounds indicating a consistent filter. These results are expected because the filter employs the identical noise statistics used to create the simulated noisy data.

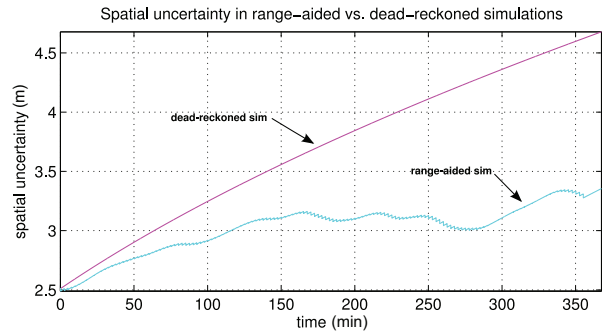


Fig. 5. The spatial uncertainty of the filter is represented here by the fourth root of the determinant of the x - y portion of the covariance matrix over the course of the dive. As expected, the spatial uncertainty in the dead-reckoned track increases monotonically over time, while the uncertainty in the range-aided trajectory is bounded as a result of the range measurements.

5. Deep-water field trials

Sea trials were conducted by the authors and collaborators during an expedition on the R/V *Knorr*, to the southern Mid-Atlantic Ridge (SMAR) in January 2008. The goal of the expedition was to test and evaluate engineering methods for locating and mapping new hydrothermal vents on the SMAR.

5.1. Site description

The SMAR is a divergent boundary between the South American Plate and the African Plate that is presently spreading at about 2.5 cm per year. The survey site, shown in Figure 8, is located near $04^\circ \text{ S } 12^\circ \text{ W}$ in a deep non-transform discontinuity whose maximum depth exceeds 4000 m (German et al. 2008). Our operations were conducted on a section of the SMAR to the north of the sites where active hydrothermal vents were first discovered by a combination of deep-tow and deep-submergence technologies culminating in photography by the autonomous underwater vehicle (AUV) *ABE* (German et al. 2008), and subsequently sampled by the remotely operated underwater vehicle (ROV) *Marum Quest* (Haase et al. 2007).

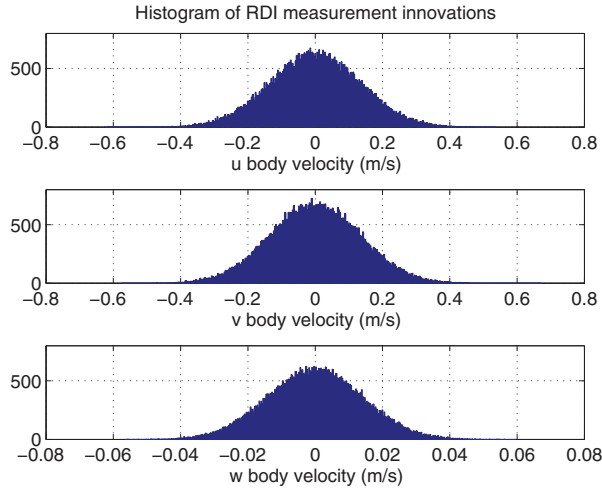


Fig. 6. The distribution of the innovations of the DVL velocity measurements are zero mean and Gaussian as expected.

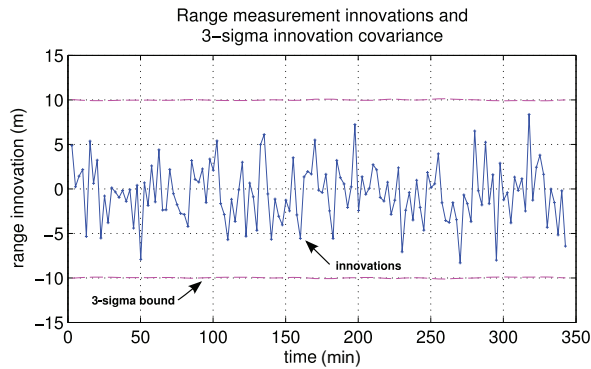


Fig. 7. The range measurement innovations from the simulated dive are well contained within the $3\text{-}\sigma$ innovation covariance bounds.

5.2. Experimental setup

The data presented in this paper were collected by the Acomms system (Webster et al. 2009a) installed on the AUV *Puma* (Singh et al. 2004), developed at WHOI, and the R/V *Knorr*. *Puma* is a 5000-m-rated AUV equipped with the following navigation sensors: a Paroscientific pressure depth sensor, an OCTANS fiber-optic gyrocompass for attitude and attitude rate measurements, and a 300-kHz RDI Doppler velocity log (DVL) for velocity measurements. The vehicle is equipped with a WHOI micro-modem (Freitag et al. 2005) and an ITC-3013 transducer (ITC 2010) for acoustic communications and range measurements. A PPSBoard was installed on the vehicle for precision timing (Eustice et al. 2006, 2007). The PPSBoard uses a low-power, temperature-compensated precision clock from SeaScan Inc. to provide precise time-keeping. The SeaScan clock has a maximum drift rate of approximately 1 ms over 14 hrs, which equates to a 1.5 m error in range—an acceptable error given the tolerances of the system. Prior

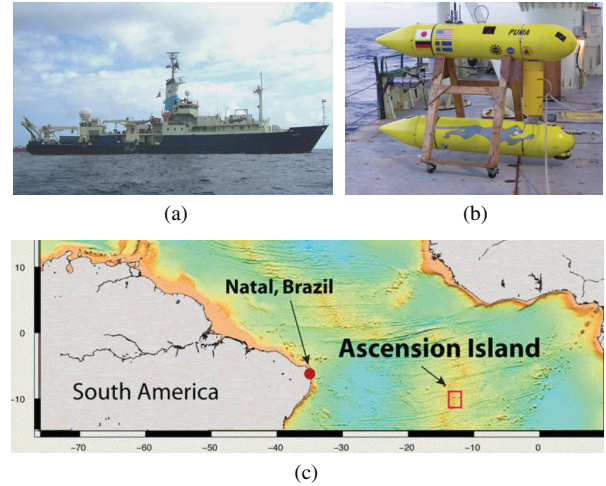


Fig. 8. (a) R/V *Knorr*. (b) AUV *Puma*. (c) The survey site is shown by the box near Ascension Island on the southern Mid-Atlantic Ridge.

to each vehicle dive, the PPSBoard was synchronized to coordinated universal time (UTC) via GPS.

The R/V *Knorr* is an 85-m-long oceanographic research vessel operated by WHOI. The ship has two azimuthing stern thrusters, a retractable azimuthing bow thruster, and dynamic positioning (DP) capability enabling it to hold station and maneuver in any direction (Woods Hole Oceanographic Institution 2010). For the ship's position information we used the C-Nav 2000 Real-Time GIPSY (RTG) GPS with a reported horizontal accuracy of 10 cm (C&C Technologies 2010). An Applanix POS/MV-320 provided heading, pitch, and roll data with a reported accuracy of 0.02° (Applanix 2008). The ship was also equipped with a WHOI micro-modem (Freitag et al. 2005) and an ITC-3013 (ITC 2010) transducer for sending and receiving acoustic data packets. Figure 8 shows the R/V *Knorr*, the AUV *Puma*, and the survey area near Ascension Island.

On *Puma* Dive 03, the vehicle conducted a survey at 3800 m depth comprising 12 tracklines approximately 65 m apart and 700 m long while maintaining an altitude of 200 m. The vehicle spent approximately 8.6 hours at depth performing the survey. While the vehicle carried out the survey mission, we repositioned the R/V *Knorr* above the survey site in a diamond shaped pattern, holding station at each apex. This was done to provide range measurements to the vehicle from different locations for increased observability (Song 1999). During these field trials we used two-way acoustic communication between the vehicle and the ship initiated by the vehicle. Acoustic data packets were sent from the vehicle to the ship and requested by the vehicle from the ship every 30 seconds.

5.3. Vehicle position initialization

Because the EKF algorithm performs linearization along the system trajectories, an initial state estimate too far from

the actual state could cause the algorithm to be unstable. In this implementation we initialized the CEKF with an MLE of the vehicle state and covariance. For this implementation of the CEKF, the maximum-likelihood estimation is performed over the entire data set as previously reported in Eustice et al. (2007). For implementation as an on-line algorithm, a real-time initialization would be necessary, such as a small-batch MLE calculated over the first few range measurements, a least mean-squares method presented in McPhail and Pebody (2009), or the hybrid particle-filter/EKF approach presented in Fallon et al. (2010). In addition, algorithms that allow the vehicle to navigate through the water column could potentially be employed to lessen the uncertainty in vehicle position accrued during the vehicle's descent to the planned survey depth (Stanway 2010).

5.4. Sensor alignment

The vehicle reference frame is defined to be coincident with the Doppler frame. Small angular offsets between the OCTANS and the Doppler are estimated in post-processing using a batch solution described in Kinsey and Whitcomb (2007). The offset— 3.5° in heading, 3.24° in pitch, and 0.64° in roll—is accounted for as a mounting offset in the OCTANS. A -1.5° mounting offset in pitch for the Doppler is estimated based on the agreement between the vertical velocity measurements of the Doppler and depth measurements from the Paroscientific pressure depth sensor.

5.5. Experimental results

The integrity of the vertical acoustic telemetry channel varied over the course of the dive. While the vehicle was surveying near the bottom, a total of 342 acoustic data packets from which we could calculate range were successfully received, all of them from the vehicle to the ship, for an average of a one-way range measurement every 90 seconds.

To investigate the effect of range measurements on the CEKF's estimate, the filter was run both without range measurements (dead-reckoning using only the vehicle-based sensor data collected during the experiment) and with range measurements (range-aided navigation). The resulting vehicle trajectories, along with the LBL fixes and the ship's track, are shown in Figure 9.

To further enable a comparison of the effect of including range measurements, Figure 10 shows the spatial uncertainty of the filter. As expected the uncertainty of the dead-reckoned trajectory increases over time, while the uncertainty in the range-aided trajectory is smaller as a result of the range measurements. The spikes in uncertainty in both trajectories are the result of the DVL dropping out for a number of measurements before being regained. Without velocity measurements, the spatial uncertainty rises quickly due to process noise, but subsequently drops when

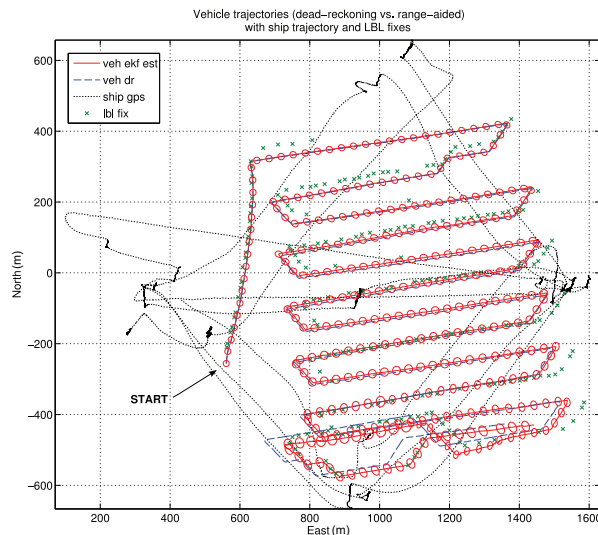


Fig. 9. Two estimated vehicle trajectories are shown: the dashed line is the dead-reckoned vehicle trajectory without range measurements, the solid line is the range-aided vehicle trajectory with $3\text{-}\sigma$ covariance ellipses. The LBL fixes are shown as x's and the ship's track is superimposed as a dotted line. The range-aided trajectory more closely follows the LBL fixes, though there is some systematic error between both trajectories and the LBL fixes.

the velocity measurements are resumed due to correlation between position and velocity.

LBL fixes provide ground truth for the estimated vehicle trajectory. Unfortunately LBL fixes were largely unavailable on tracklines where the vehicle was heading East, as shown in Figure 9, most likely due to shadowing of the transducer by the vehicle frame at this vehicle heading. A histogram of the difference between the range-aided trajectory and the LBL fixes, where available, is shown in Figure 11. Table 2 shows the average difference between the CEKF estimate and the LBL estimate of vehicle position for the range-aided trajectory and the dead-reckoned trajectory, respectively. The range-aided trajectory has smaller errors and variances in most cases; however, the non-zero mean suggests the presence of additional systematic errors that are not accounted for in the reported sensor calibrations. We believe that the difference is partly due to LBL calibration, described in Section 5.6 below, and partly due to unaccounted-for sensor offsets in the vehicle sensors.

We use innovations from the sensor measurements to test the consistency of the CEKF. Histograms of the innovations of the DVL velocity measurements are shown in Figure 12. The distribution of all three of the velocity measurements are approximately zero-mean, and the distribution of the u and v velocity innovations both appear Gaussian. The w velocity distribution is not Gaussian, indicating that there may be a small mounting offset in the Doppler pitch, causing a discrepancy between the actual versus the measured vertical velocity of the vehicle, or a mismatch between the depth sensor and the vehicle's vertical velocity.

Table 2. Difference between CEKF estimated trajectories and LBL estimates.

| | Range-aided trajectory versus LBL estimates | | | |
|----------|---------------------------------------------|-------------|----------|-------|
| | Relative | | Absolute | |
| | Across-track | Along-track | North | East |
| Mean (m) | −18.4 | 18.8 | −16.1 | −29.2 |
| Std (m) | 24.3 | 16.8 | 10.3 | 18.5 |

| | Dead-reckoned trajectory versus LBL estimates | | | |
|----------|-----------------------------------------------|-------------|----------|-------|
| | Relative | | Absolute | |
| | Across-track | Along-track | North | East |
| Mean (m) | −19.8 | 19.2 | −16.2 | −36.5 |
| Std (m) | 29.8 | 20.3 | 9.12 | 19.4 |

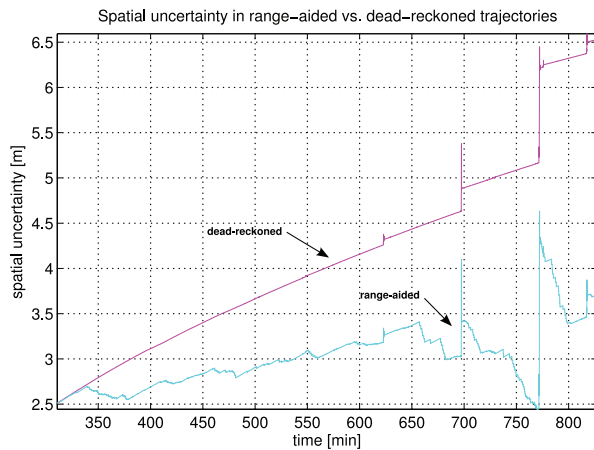


Fig. 10. As in Figure 5, the spatial uncertainty of the filter is represented by the fourth root of the determinant of the x - y portion of the covariance matrix over the course of the dive. As expected, the spatial uncertainty in the dead-reckoned track is unbounded over time, while the range-aided trajectory has bounded uncertainty as a result of the range measurements. The spikes in uncertainty in both trajectories are the result of the DVL dropping out for a number of measurements before being regained. Without velocity measurements, the uncertainty rises quickly due to process noise, but subsequently drops when the velocity measurements are resumed.

5.6. Errors in ground truth from long baseline

While submerged, the vehicle used range information in the form of two-way travel times from three LBL beacons to estimate its absolute position in real time (Hunt et al. 1974). The position fixes from LBL also provide the baseline for the OWTT navigation filter—we compared the filter's estimated vehicle position to the position fixes from LBL as a measure of the algorithm's accuracy. The accuracy of the vehicle's position estimates from LBL

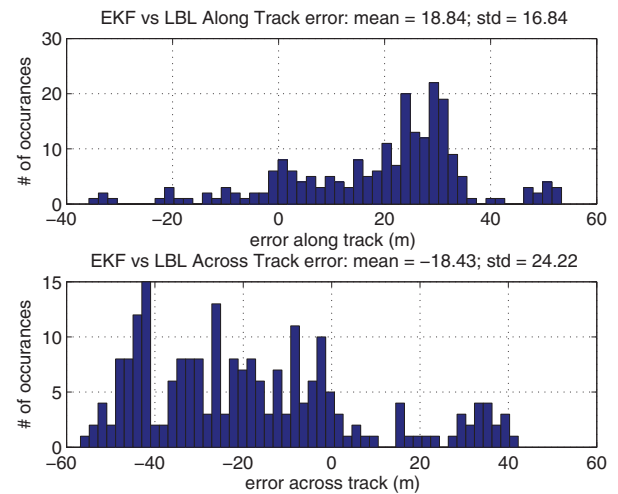
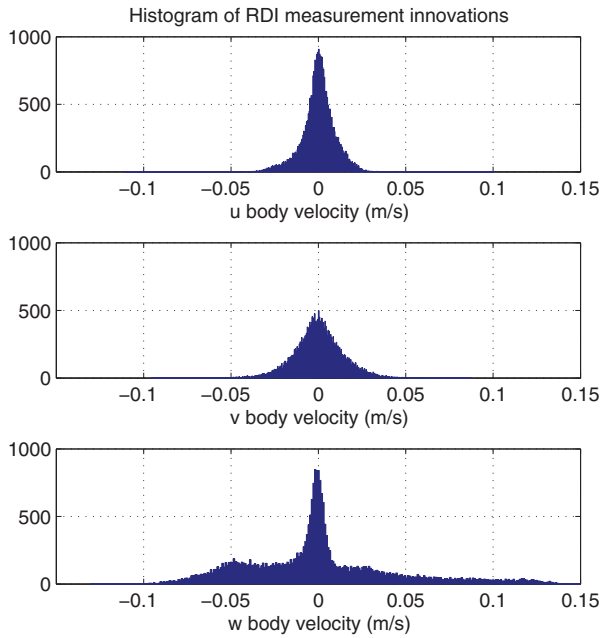


Fig. 11. The distribution of the along-track and across-track components of the difference between the LBL fixes and the range-aided estimate of vehicle position shows a systematic bias. The mean and standard deviation for the components are given in the plot titles.

ranges, however, is predicated on the accuracy to which the position of the LBL beacons is known—uncertainty in beacon location translates directly to uncertainty in the vehicle's position estimate in the radial direction from the beacon. The LBL beacon survey on this expedition used the standard procedure of collecting two-way travel times from the ship to the individual beacons from 5–10 different ship locations after each beacon reached the seafloor. The ship locations are spaced approximately equally around a circle with ~ 1 km horizontal radius from each beacon's ground truth drop location. Beacon location is then estimated using a least-squares algorithm after outliers have been manually rejected. Table 3 shows the position of the three LBL beacons relative to the vehicle's survey site and the residual

Table 3. LBL beacon location and accuracy of position estimate.

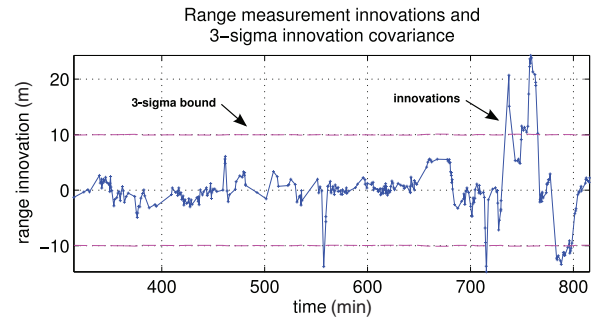
| Beacon | Approximate location | RMS error |
|--------|----------------------|-----------|
| A | 3 km west | 1.8 m |
| B | 3 km north | 3.8 m |
| C | 2.5 km east | 3.7 m |

**Fig. 12.** The distribution of the innovations of the DVL velocity measurements show that all are zero-mean and the u and v innovations are Gaussian distributed as expected. The non-Gaussian nature of the w velocity distribution may indicate a small mounting offset in the pitch of the DVL instrument, causing a discrepancy between the actual versus the measured vertical velocity.

root mean squared error of the estimated beacon position from the LBL beacon survey.

5.7. Errors in acoustic range measurements

In the Kalman filter, both the process noise and the sensor measurement noise are assumed to be zero-mean and Gaussian. Non-zero-mean or non-Gaussian noise violates this assumption and is a source of error in the filter's estimate. Vehicle-based navigation sensors, such as the OCTANS gyrocompass, the Doppler velocity log, and the pressure depth sensor, are commonly used and well characterized, such that, when calibrated properly, they can be modeled acceptably as having Gaussian noise. The exception is that mounting offsets, as noted in Section 5.4, can cause bias in the sensor measurements if not properly accounted for. In contrast, acoustic range measurements are often not Gaussian distributed because of factors such as ray-bending of the acoustic signal as it passes through the water column and false range measurements caused by acoustic multi-path.

**Fig. 13.** The innovations in the range measurements over the course of the survey show that until around a mission time of 700 minutes the range measurements are consistent with the $3\text{-}\sigma$ innovation covariance (dashed lines), but exceed the $3\text{-}\sigma$ bounds near the end of the survey.

Figures 13 and 14 show the innovations for the 342 range measurements made during the vehicle's survey plotted both over time and in a histogram, respectively. Figure 13 shows that for the majority of the survey the range measurements are consistent with the $3\text{-}\sigma$ innovation covariance (dashed lines), but exceed the $3\text{-}\sigma$ bounds near the end of the survey. Several factors could have caused errors in the range measurements during this time. The group of range measurements that exceed the positive $3\text{-}\sigma$ bound (mission time 749 to 766 min) were made while the ship was at the western apex of its diamond pattern, moving west. The group of range measurements that exceed the negative $3\text{-}\sigma$ bound (mission time 784 to 798 min) were made while the ship was at the eastern apex of the diamond, moving north. The respective location of the ship and the sign of the innovation could indicate an error in estimated vehicle position. In addition, because the modem was not rigidly attached to the ship but lowered over the side on a cable, the motion of the ship, and resulting movement in the modem transducer, may have affected the fidelity of the range measurements. In comparison to the experimental innovations, the innovations of the range measurements for the simulated dive are well contained within the $3\text{-}\sigma$ innovations covariance bounds for the duration of the dive, as shown in Figure 7.

Because the Kalman filter framework relies on the assumption of Gaussian noise, we have assumed a large standard deviation for the range measurement noise in the filter model (3.3 m, see Table 1) to mitigate the non-Gaussian nature of the measurement noise. We explore several factors that could cause the non-Gaussian range measurement noise.

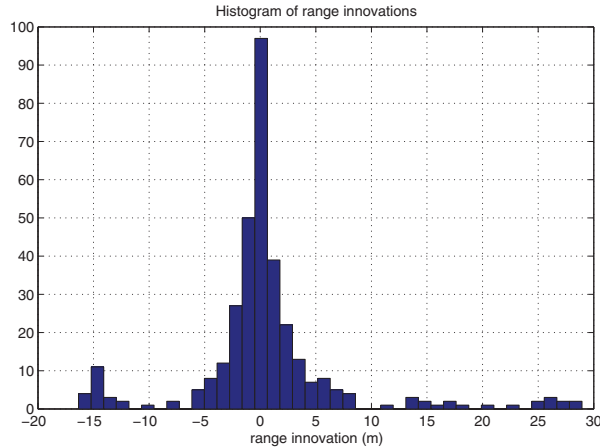


Fig. 14. The distribution of the range-measurement innovations shows the range measurements are near zero-mean but not Gaussian distributed.

Sound velocity estimation. In this implementation, the CEKF uses a depth-weighted average sound velocity to calculate the range from the travel time of the acoustic data packets. The actual sound velocity profile, however, varies over depth as shown in Figure 15. Refraction due to the change in sound speed with depth can cause ray bending in acoustic signals transmitted through the water column (Urick 1983). As a result, the travel time of an acoustic signal is not directly proportional to slant range and is dependent on the distance and horizontal displacement between the vehicle and the ship.

To quantify this error, we consider a range estimate between the vehicle and the ship when the ship is at the western-most apex of its diamond pattern and the vehicle is at the far eastern edge of its survey, thus incorporating the largest horizontal offset possible (1236 m). Calculating the difference in the range estimate found using ray-bending techniques (Schmidt 2009) versus the depth-weighted average sound velocity, we find that the model incurs an error in the range estimate of the order of one meter. Ray-bending, therefore, is not likely to be a substantial source of error in this data set. In future work, adding a range-dependent component for the range measurement noise model would be appropriate, especially for shallow applications where there is a larger relative horizontal offset and the distance between the vehicle and the ship changes more significantly throughout the dive.

Acoustic multi-path. Multi-path errors can cause large errors in range measurements when the acoustic signal bounces off the surface of the seafloor one or more times before reaching the vehicle. If the vehicle and ship configuration is static or changes slowly, then multi-path error can show up repeatably, causing a multi-modal error distribution. Multi-path errors are typically worse in shallow-water deployments where the angle of incidence between the acoustic signal and the surface or the seafloor is very large.

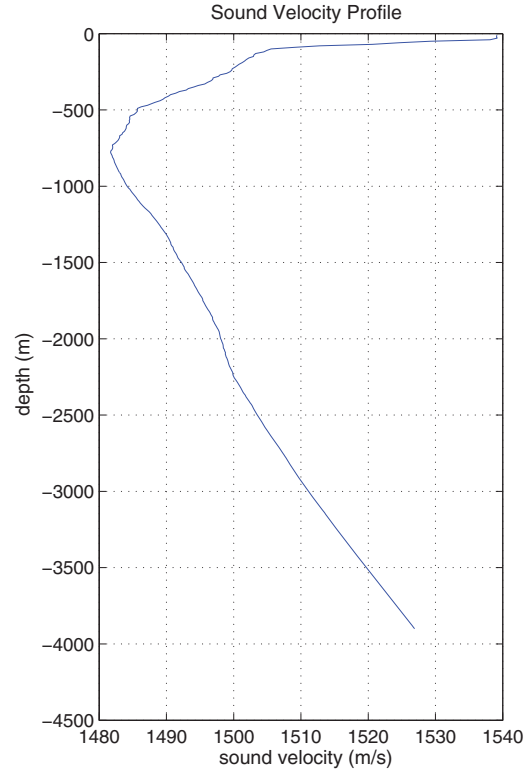


Fig. 15. Sound velocity profile computed from data from the conductivity-temperature-depth (CTD) sensor on *Puma*.

In this deployment, because the vehicle was close to vertical underneath the ship, we did not experience noticeable problems from acoustic multi-path.

Ship GPS drift and correlation. Position measurements from a GPS are subject to drift and correlation when the satellite constellation changes position and geometry, and when the satellites appear and disappear from the line of sight. The horizontal dilution of precision (HDOP) reported by the GPS sensor indicates the accuracy of the current measurement based upon the geometry of the satellites. HDOP is a scale factor for the GPS sensor's nominal accuracy, such that if σ_{nom} is the nominal standard deviation of horizontal measurements provided by the GPS sensor (as reported by the manufacturer), then the actual standard deviation of the horizontal measurement is $\text{HDOP} \times \sigma_{\text{nom}}$ (Hofman-Wellenhof et al. 1994). Thus $\text{HDOP} = 1$ indicates ideal geometry and measurements that are as accurate as possible for the sensor, and higher values indicate worse performance. A histogram of the HDOP values reported by the ship's GPS over the course of the dive is shown in Figure 16.

Given that the GPS used during this experiment has a reported horizontal accuracy of less than 10 cm (C&C Technologies 2010), and 98% of the measurements have an HDOP of 2 or less, we conclude that any drift or correlation in the GPS data is not a significant source of error in this data set.

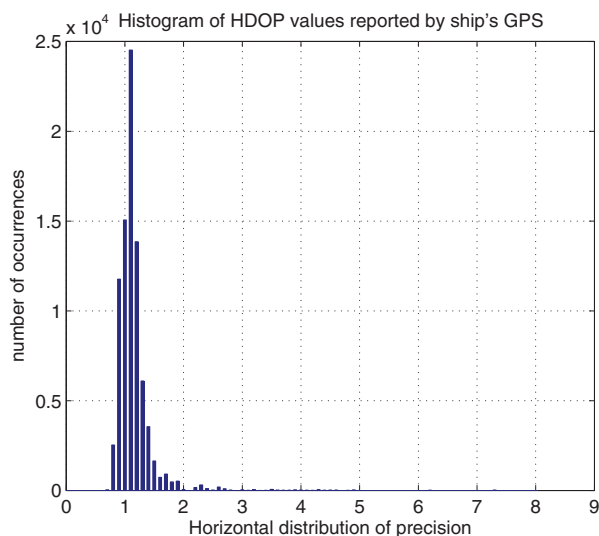


Fig. 16. The distribution of horizontal dilution of precision (HDOP) reported by the GPS receiver on the ship, showing an HDOP of 2 or less for 98% of the reported measurements for the duration of the dive.

6. Discussion and conclusions

This paper reports the design and implementation of a CEKF that estimates the position of a vehicle using vehicle-based navigation sensors and range measurements between the vehicle and a reference beacon based on the one-way travel time of acoustic data packets. The filter is designed for a moving reference beacon and a single vehicle but can be extended trivially to incorporate any number of vehicles and range measurements between them. The CEKF relies on concurrent access to the sensor measurements and thus is applicable in post-processing.

The goal of this work is to report and evaluate with experimental deep-water survey data a new OWTT navigation method utilizing a centralized delayed-state EKF. Simulation and deep-water sea trials evaluating single-beacon one-way-travel-time navigation implemented with a CEKF were shown. Experimental results from the CEKF compared to the ground truth absolute-navigation from LBL position fixes show that the difference between the CEKF results and LBL is commensurate with the errors we typically expect from LBL. We conclude that single-beacon navigation is a viable alternative to LBL navigation for deep-water applications where the ship or surface node can be moved around the survey site to provide appropriate geometric constraints on the vehicle's position estimate. These results expand upon those reported in Eustice et al. (2006) and Eustice et al. (2007), which reported results from single-beacon one-way-travel-time acoustic navigation in shallow water.

Future research in single-beacon navigation will focus on the decentralized real-time implementation to support simultaneous multi-vehicle navigation. The CEKF reported herein will serve as the benchmark for future Kalman-filter-based decentralized estimators.

Funding

This work was supported by the National Science Foundation [NSF Awards ATM-0427220, ATM-0428122, IIS-0746455, and IIS-0812138].

Acknowledgments

The authors are grateful to Clay Kunz and Chris Murphy for their support of *Puma* software, to Dr Michael C Jakuba for his support of the reported LBL navigation, and to Dr James C Kinsey for his help with sensor calibrations. The authors are also grateful to Captain George Silva, the officers, and crew of the R/V *Knorr* for their exemplary support.

References

- Alleyne JC (2000) Position estimation from range only measurements. Master's Thesis, Naval Postgraduate School, Monterey, CA, US.
- Applanix (2008) POS MV (Position and Orientation Systems for Marine Vessels). Applanix, Richmond Hill, ON, Canada. Available at: <http://www.applanix.com/products/marine/pos-mv.html> (accessed 14 November 2010).
- Baccou P and Jouvencel B (2002) Homing and navigation using one transponder for AUV, postprocessing comparisons results with long base-line navigation. In: *Proceedings of the IEEE international conference on robotics and automation (ICRA)*, Washington, DC, May 2002, vol. 4, pp. 4004–4009.
- Baccou P and Jouvencel B (2003) Simulation results, post-processing experimentations and comparisons results for navigation, homing and multiple vehicles operations with a new positioning method using on transponder. In: *Proceedings of the IEEE/RSJ international conference on intelligent robots and systems (IROS)*, Las Vegas, NV, October 2003, vol. 1, pp. 811–817.
- Bahr A (2009) Cooperative localization for autonomous underwater vehicles. PhD Dissertation, Massachusetts Institute of Technology, Cambridge, MA, USA.
- Bahr A and Leonard J (2006) Cooperative localization for autonomous underwater vehicles. In: *Proceedings of the 10th international symposium on experimental robotics (ISER)*, Rio de Janeiro, Brazil, July 2006, pp. 387–395.
- Bar-Shalom Y, Rong Li X and Kirubarajan T (2001) *Estimation with Applications to Tracking and Navigation*. New York: John Wiley & Sons, Inc.
- C&C Technologies (2010) *C-Nav2000*. C&C Technologies, Lafayette, LA, USA. Available at: <http://www.cnavgns.com/site407.php> (accessed 14 November 2010).
- Eustice RM (2005) Large-area visually augmented navigation for autonomous underwater vehicles. PhD dissertation, Massachusetts Institute of Technology and Woods Hole Oceanographic Institution.
- Eustice RM, Whitcomb LL, Singh H and Grund M (2006) Recent advances in synchronous-clock one-way-travel-time acoustic navigation. In: *Proceedings of the IEEE/MTS OCEANS conference and exhibition*, Boston, MA, USA, September 2006, pp. 1–6.

- Eustice RM, Whitcomb LL, Singh H and Grund M (2007) Experimental results in synchronous-clock one-way-travel-time acoustic navigation for autonomous underwater vehicles. In: *Proceedings of the IEEE international conference on robotics and automation (ICRA)*, Rome, Italy, April 2007, pp. 4257–4264.
- Fallon MF, Papadopoulos G, Leonard JJ and Patrikalakis NM (2010) Cooperative AUV navigation using a single maneuvering surface craft, *International Journal of Robotics Research* 29(12): 1461–1474.
- Freitag L, Grund M, Singh S, Partan J, Koski P and Ball K (2005) The WHOI micro-modem: An acoustic communications and navigation system for multiple platforms. In: *Proceedings of the IEEE/MTS OCEANS conference and exhibition*, Washington, DC, September 2005, pp. 1086–1092.
- Gadre A (2007) Observability analysis in navigation systems with an underwater vehicle application. PhD dissertation, Virginia Polytechnic Institute and State University, Blacksburg, Virginia.
- Gadre AS and Stilwell DJ (2004) Toward underwater navigation based on range measurements from a single location. In: *Proceedings of the IEEE international conference on robotics and automation (ICRA)*, New Orleans, LA, April 2004, pp. 4472–4477.
- Gadre A and Stilwell D (2005a) A complete solution to underwater navigation in the presence of unknown currents based on range measurements from a single location. In: *Proceedings of the IEEE/RSJ international conference on intelligent robots and systems (IROS)*, Edmonton, AB, Canada, August 2005, pp. 1420–1425.
- Gadre A and Stilwell D (2005b) Underwater navigation in the presence of unknown currents based on range measurements from a single location. In: *Proceedings of the American control conference*, June 2005, vol. 1, pp. 656–661.
- Gelb A, ed. (1982) *Applied Optimal Estimation*. Cambridge, MA: MIT Press.
- German C, Bennett S, Connelly D, Evans A, Murton B, Parson L, Prien R, Ramirez-Llodra E, Jakuba M, Shank T, Yoerger D, Baker E, Walker S and Nakamura K (2008) Hydrothermal activity on the southern Mid-Atlantic Ridge: Tectonically- and volcanically-controlled venting at 4–5°S. *Earth and Planetary Science Letters* 273(3–4): 332–344.
- Haase KM, et al. (2007) Young volcanism and related hydrothermal activity at 5°S on the slow-spreading southern Mid-Atlantic Ridge. *Geochemistry, Geophysics, Geosystems* 8: Q11002.
- Hartsfield JC (2005) Single transponder range only navigation geometry (STRONG) applied to REMUS autonomous underwater vehicles. Master's Thesis, Massachusetts Institute of Technology and Woods Hole Oceanographic Institution.
- Hofman-Wellenhof B, Lichtenegger H and Collins J (1994) *Global Positioning System: Theory and Practice*, 3rd ed. New York: Springer-Verlag.
- Hunt M, Marquet W, Moller D, Peal K, Smith W and Spindel R (1974) An acoustic navigation system. Technical report WHOI-74-6, Woods Hole Oceanographic Institution, December.
- ITC (2010) *Model ITC-3013*. International Transducer Corporation, Santa Barbara, CA, USA. Available at: <http://www.itc-transducers.com/> (accessed 14 November 2010).
- Jouffroy J and Reger J (2006) An algebraic perspective to single-transponder underwater navigation. In: *Proceedings IEEE 2006 CCA/CACSD/ISIC*, Munich, Germany, October 2006, pp. 1789–1794.
- Kalman RE (1960) A new approach to linear filtering and prediction problems. *Transactions of the ASME—Journal of Basic Engineering* 82(D): 35–45.
- Kinsey JC and Whitcomb LL (2007) In situ alignment calibration of attitude and Doppler sensors for precision underwater vehicle navigation: Theory and experiment. *IEEE Journal of Oceanic Engineering* 32(2): 286–299.
- LaPointe CE (2006) Virtual long baseline (VLBL) autonomous underwater vehicle navigation using a single transponder. Master's thesis, Massachusetts Institute of Technology and Woods Hole Oceanographic Institution.
- Larsen M (2000) Synthetic long baseline navigation of underwater vehicles. In: *Proceedings of the IEEE/MTS OCEANS conference and exhibition*, Providence, RI, USA, September 2000, vol. 3, pp. 2043–2050.
- Larsen MB (2001) Autonomous navigation of underwater vehicles. PhD Dissertation, Technical University of Denmark, Denmark.
- Larsen MB (2002) High performance autonomous underwater navigation. *Hydro International* 6: 2043–2050.
- Lee P-M, Jun B-H and Lim Y-K (2008) Review on underwater navigation system based on range measurements from one reference. In: *Proceedings of the IEEE/MTS OCEANS conference and exhibition*, Kobe, Japan, April 2008, pp. 1–5.
- McPhail S and Pebody M (2009) Range-only positioning of a deep-diving autonomous underwater vehicle from a surface ship. *IEEE Journal of Oceanic Engineering* 34(4): 669–677.
- Morice CP and Veres SM (2011) Geometric bounding techniques for underwater localization using range-only sensors. *Proceedings of the Institution of Mechanical Engineers, Part I: Journal of Systems and Control Engineering* 225(1): 74–84.
- Ristic B, Arulampalam S and McCarthy J (2002) Target motion analysis using range-only measurements: Algorithms, performance and application to ISAR data. *Signal Processing* 82(2): 273–296.
- Ross A and Jouffroy J (2005) Remarks on the observability of single beacon underwater navigation. In: *Proceedings of the international symposium on unmanned untethered submersible technology (UUST)*, August 2005.
- Scherbatyuk A (1995) The AUV positioning using ranges from one transponder LBL. In: *Proceedings of the IEEE/MTS OCEANS conference and exhibition*, San Diego, CA, USA, vol. 3, pp. 1620–1623.
- Schmidt V (2009) Matlab® raytrace.m function. Center for Coastal and Ocean Mapping/Joint Hydrographic Center, University of New Hampshire, Durham, NH, USA. Available at: <http://www.mathworks.com/matlabcentral/fileexchange/26253-raytrace> (accessed 14 November 2010).
- Singh H, Bellingham J, Hover F, Lerner S, Moran B, von der Heydt K and Yoerger D (2001) Docking for an autonomous ocean sampling network. *IEEE Journal of Oceanic Engineering* 26(4): 498–514.
- Singh H, Can A, Eustice RM, Lerner S, McPhee N, Pizarro O and Roman C (2004) SeaBED AUV offers new platform for high-resolution imaging. *EOS, Transactions of the American Geophysical Union* 85(31): 289, 294–295.
- Song T (1999) Observability of target tracking with range-only measurements. *IEEE Journal of Oceanic Engineering* 24(24): 383–387.

- Stanway M (2010) Water profile navigation with an acoustic Doppler current profiler. In: *Proceedings of the IEEE/MTS OCEANS conference and exhibition*, Sydney, Australia, May 2010, pp. 1–5.
- Urick R (1983) *Principles of Underwater Sound*. McGraw-Hill, Inc.
- Vaganay J, Baccou P and Jouvencel B (2000) Homing by acoustic ranging to a single beacon. In: *Proceedings of the IEEE/MTS OCEANS conference and exhibition*, Providence, RI, USA, September 2000, vol. 2, pp. 1457–1462.
- Walls JM and Eustice RM (2011) Experimental comparison of synchronous-clock cooperative acoustic navigation algorithms. In: *Proceedings of the IEEE/MTS OCEANS conference and exhibition*, Kona, HI, USA, pp. 1–7.
- Webster SE (2010) Decentralized single-beacon acoustic navigation: Combined communication and navigation for underwater vehicles. PhD dissertation, Johns Hopkins University, Baltimore, MD, USA.
- Webster SE, Eustice RM, Murphy C, Singh H and Whitcomb LL (2009) Toward a platform-independent acoustic communications and navigation system for underwater vehicles. In: *Proceedings of the IEEE/MTS OCEANS conference and exhibition*, Biloxi, MS, USA, October 2009, pp. 1–7.
- Webster SE, Eustice RM, Singh H and Whitcomb LL (2009) Preliminary deep water results in single-beacon one-way-travel-time acoustic navigation for underwater vehicles. In: *Proceedings of the IEEE/RSJ international conference on intelligent robots and systems (IROS)*, St. Louis, MO, USA, October 2009, pp. 2053–2060.
- Webster SE, Whitcomb LL and Eustice RM (2010) Preliminary results in decentralized estimation for single-beacon acoustic underwater navigation. In: *Proceedings of the robotics: Science and systems conference*, Zaragoza, Spain, June 2010.
- Woods Hole Oceanographic Institution (2010) R/V *Knorr*: Specifications. Woods Hole, MA. Available at: <http://www.whoi.edu/page.do?pid=8496> (accessed 14 November 2010).

A. Review of EKF formulation

The EKF applies the general approach of the Kalman filter (Kalman 1960) to non-linear plants by linearizing the plant process and observation models along the trajectory of the system. The formulation reported here is for a non-linear plant with discrete observations (Gelb 1982). Consider the general non-linear plant process and observation model

$$\dot{\mathbf{x}}(t) = \mathbf{f}(\mathbf{x}(t), t) + \mathbf{G}(t) \mathbf{w}(t) + \mathbf{u}(\mathbf{x}(t), t) \quad (35)$$

$$\mathbf{z}_k = \mathbf{h}(\mathbf{x}(t_k)) + \mathbf{v}_k, \quad k = 1, 2, \dots \quad (36)$$

where $\mathbf{x}(t)$ is the state in continuous time, $\mathbf{u}(\mathbf{x}(t), t)$ is the input, \mathbf{z}_k is the measurement at time step t_k in discrete time, and $\mathbf{w}(t) \sim \mathcal{N}(0, \mathbf{Q}(t))$ and $\mathbf{v}_k \sim \mathcal{N}(0, \mathbf{R}_k)$ are independent zero-mean Gaussian process noise and measurement noise, respectively.

The CEKF reported herein employs a discrete-time linearization of the process model, whose general form is

$$\mathbf{x}_{k+1} = \mathbf{F}_k \mathbf{x}_k + \mathbf{B}_k \mathbf{u}_k + \mathbf{w}_k \quad (37)$$

to recursively estimate the mean, $\boldsymbol{\mu}$, and covariance, $\boldsymbol{\Sigma}$, of the state vector \mathbf{x}

$$\boldsymbol{\mu} = E[\mathbf{x}] \quad (38)$$

$$\boldsymbol{\Sigma} = E[(\mathbf{x} - \boldsymbol{\mu})(\mathbf{x} - \boldsymbol{\mu})^\top], \quad (39)$$

resulting in the general form of the process prediction equations

$$\boldsymbol{\mu}_{k+1|k} = \mathbf{F}_k \boldsymbol{\mu}_{k|k} + \mathbf{B}_k \mathbf{u}_k \quad (40)$$

$$\boldsymbol{\Sigma}_{k+1|k} = \mathbf{F}_k \boldsymbol{\Sigma}_{k|k} \mathbf{F}_k^\top + \mathbf{Q}_k \quad (41)$$

where \mathbf{F}_k is the discrete-time linear state transition matrix, \mathbf{B}_k is the discrete-time linear input matrix, \mathbf{Q}_k is the discrete-time process noise covariance, \mathbf{u}_k is the piecewise-constant input at time step t_k , and we use \top as the transpose operator.

The measurement update equations for the EKF are

$$\boldsymbol{\mu}_{k|k} = \boldsymbol{\mu}_{k|k-1} + \mathbf{K}_k (\mathbf{z}_k - \mathbf{h}_k(\boldsymbol{\mu}_{k|k-1})) \quad (42)$$

$$\begin{aligned} \boldsymbol{\Sigma}_{k|k} &= \boldsymbol{\Sigma}_{k|k-1} - \mathbf{K}_k \mathbf{H}_k \boldsymbol{\Sigma}_{k|k-1} \\ &= (\mathbf{I} - \mathbf{K}_k \mathbf{H}_k) \boldsymbol{\Sigma}_{k|k-1} \end{aligned} \quad (43)$$

where \mathbf{H}_k is the Jacobian of \mathbf{h} at time step t_k

$$\mathbf{H}_k = \left. \frac{\partial \mathbf{h}(\mathbf{x}(t_k))}{\partial \mathbf{x}(t_k)} \right|_{\mathbf{x}(t_k) = \boldsymbol{\mu}_{k|k-1}} \quad (44)$$

and \mathbf{K}_k is the Kalman gain at time step t_k , given by

$$\mathbf{K}_k = \boldsymbol{\Sigma}_{k|k-1} \mathbf{H}_k^\top (\mathbf{H}_k \boldsymbol{\Sigma}_{k|k-1} \mathbf{H}_k^\top + \mathbf{R}_k)^{-1}. \quad (45)$$

B. Variance of discretized process noise

To calculate the variance of the discretized vehicle process noise, equation (20), we make use of the facts that the expected value can be brought inside the integral because it is a linear operator and that the noise vector \mathbf{w}_v is independent and identically distributed in time so that the covariance $E[\mathbf{w}_v(\tau) \mathbf{w}_v^\top(\gamma)]$ is zero except when $\gamma = \tau$:

$$\begin{aligned} E[\mathbf{w}_{v_k} \mathbf{w}_{v_k}^\top] &= E \left[\int_0^T e^{\mathbf{F}_v(T-\tau)} \mathbf{G}_v \mathbf{w}_v(\tau) d\tau \int_0^T \left(e^{\mathbf{F}_v(T-\gamma)} \mathbf{G}_v \mathbf{w}_v(\gamma) \right)^\top d\gamma \right] \\ &= E \left[\int_0^T \int_0^T e^{\mathbf{F}_v(T-\tau)} \mathbf{G}_v \mathbf{w}_v(\tau) \mathbf{w}_v^\top(\gamma) \mathbf{G}_v^\top e^{\mathbf{F}_v^\top(T-\gamma)} d\tau d\gamma \right] \\ &= \int_0^T \int_0^T e^{\mathbf{F}_v(T-\tau)} \mathbf{G}_v E[\mathbf{w}_v(\tau) \mathbf{w}_v^\top(\gamma)] \mathbf{G}_v^\top e^{\mathbf{F}_v^\top(T-\gamma)} d\tau d\gamma \\ &\quad \underbrace{\mathbf{Q}_v \delta(\tau - \gamma)} \\ &= \int_0^T e^{\mathbf{F}_v(T-\tau)} \mathbf{G}_v \mathbf{Q}_v \mathbf{G}_v^\top e^{\mathbf{F}_v^\top(T-\tau)} d\tau. \end{aligned}$$